Ionics (2015) 21:3185–3192
DOI 10.1007/s11581-015-1520-1

ORIGINAL PAPER

Fe@Ag nanoparticles decorated reduced graphene oxide as ultrahigh capacity anode material for lithium-ion battery

Necip Atar[1] · Tanju Eren[1] · Mehmet Lütfi Yola[2] · Hüsnü Gerengi[3] · Shaobin Wang[4]

Received: 13 June 2015 / Revised: 9 July 2015 / Accepted: 18 July 2015 / Published online: 30 July 2015

Abstract In the present study, we report the synthesis of Fe@Ag nanoparticles/2-aminoethanethiol functionalized reduced graphene oxide (rGO) composite (Fe@AuNPs-AETrGO) and its application as an improved anode material for lithium-ion batteries (LIBs). The structure of the Fe@AgNPs-AETrGO composite was characterized by transmission electron microscopy (TEM), X-ray diffraction (XRD), scanning electron microscopy (SEM), and X-ray photoelectron spectroscopy (XPS). The electrochemical performance was investigated at different charge/discharge current rates by using CR2032 coin-type cells and cyclic voltammetry (CV). It was found that the spherical Fe@AuNPs were highly dispersed on the rGO sheets. Moreover, the Fe@AuNPs-AETrGO composite showed high specific gravimetric capacity of about 1500 mAh g^{-1} and long-term cycle stability.

Keywords Reduced graphene oxide · Metal nanoparticle · Core-shell · Anode · Lithium-ion battery

✉ Necip Atar
necipatar@gmail.com

✉ Shaobin Wang
shaobin.wang@curtin.edu.au

[1] Department of Chemical Engineering, Pamukkale University, Denizli, Turkey

[2] Department of Metallurgical and Materials Engineering, Sinop University, Sinop, Turkey

[3] Corrosion Research Laboratory, Kaynasli Vocational College, Duzce University, Kaynasli, Duzce 81900, Turkey

[4] Department of Chemical Engineering, Curtin University, GPO Box U1987, Perth, WA 6845, Australia

Introduction

In recent decades, there have been many reports on energy storage devices with high energy density and long cycle life [1]. Lithium-ion batteries (LIBs) have been applied as an important power source owing to their high operating voltage and high energy density [2]. LIBs enable to improve the energy and power density for different kinds of application such as portable electronic devices, power tools, and electric vehicles [3–5]. Currently, the fossil fuel has been used for high energy consumption [6]. The LIBs are one of the most important energy storage systems from renewable sources [7–9]. For these applications, LIBs must possess higher electrical/ionic conductivity, cycling stability, rate capability, and low cost.

The performance of LIBs depends on the cathode and anode materials. In this respect, the use of carbon-based anode materials [10], containing carbon fibers [11], carbon nanotubes [12], and graphene [8, 13], could benefit the LIBs in terms of specific capacity and cycle stability [14]. Different investigations on graphene and reduced graphene oxide (rGO) for electrochemical energy storage [8], electronics [15], and biosensors applications [16] have been reported. Furthermore, rGO has been proposed as a potential electrode material for LIBs because of its chemical structure [8], flexibility [17], high surface area [18], and electrical conductivity [19]. Moreover, different investigations on nanoparticle-based nanocomposites for electrochemical energy storage, biosensors, and electronics applications have been reported [20–28]. There are some composites based on carbon materials functionalized by nanoparticles such as Si and Au. In addition, Fe_3O_4 [29–31] was used as an anode material [32, 33] to increase the performance of LIBs. The bimetallic core@shell nanoparticles can be well controlled and their morphologies show important physicochemical properties [34, 35], which has

made the core@shell nanoparticles to be widely used in catalysis [36] and electronics [37]. Obviously, the critical factors influencing the performance of LIBs are size and shape of the nanoparticles and surface properties. In our study, Fe@Ag nanoparticles/2-aminoethanethiol functionalized rGO composite as an anode material was developed for the first time and applied for lithium-ion batteries.

Experimental

Apparatus and reagents

All chemicals in the experiments were reagent grade and were used as received. They are lithium metal foil (99.9 %, 150 μm, Sigma-Aldrich, USA), isopropyl alcohol (IPA, Sigma-Aldrich, USA), silver nitrate ($AgNO_3$, Sigma-Aldrich, USA), ascorbic acid ($C_6H_8O_6$, Sigma-Aldrich, USA), HPLC-grade acetonitrile (MeCN, Sigma-Aldrich, USA), activated carbon (Sigma-Aldrich, USA), iron (III) nitrate ($Fe(NO_3)_3$, Merck, Germany), 2-aminoethanethiol (AET, Sigma-Aldrich, USA), carbon black (Merck, Germany), polyvinylidene fluoride (PVDF, Sigma-Aldrich, USA), *N*-methyl-2-pyrrolidone (NMP, Sigma-Aldrich, USA), Cu foil (18 μm), lithium hexafluorophosphate ($LiPF_6$, Merck, Germany), ethylene carbonate (EC, Merck, Germany), dimethyl carbonate (DMC, Merck, Germany), sulfuric acid (H_2SO_4, Merck, Germany), potassium persulfate ($K_2S_2O_8$, Merck, Germany), phosphorus pentoxide (P_2O_5, Merck, Germany), graphite powder (Merck, Germany), potassium permanganate ($KMnO_4$, Merck, Germany), hydrogen peroxide (H_2O_2, Merck, Germany), ethanol (Merck, Germany), hydrochloric acid (HCl, Sigma-Aldrich, USA), and *N*-(3-dimethylaminopropyl)-*N*′-ethylcarbodiimide hydrochloride (EDC, Sigma-Aldrich, USA). The ultra-pure water with resistance of 18.3 MΩ cm (Human Power 1^+ Scholar purification system, Korea) was used for the experiments of aqueous media.

JEOL 2100 HRTEM (JEOL Ltd., Tokyo, Japan) and ZEISS EVO 50 SEM (Germany) analytic microscopies were used to investigate the morphology of Fe@AgNPs-AETrGO composite. Scanning electron microscopy (SEM) images were obtained on a ZEISS EVO 50 analytic microscope (Germany).

X-ray photoelectron spectroscopy (XPS) analysis was performed on a PHI 5000 Versa Probe (Φ ULVAC-PHI, Inc., Japan/USA) model with monochromatized Al Kα radiation (1486.6 eV) as an X-ray anode operated at 50 W. To prepare the sample, one drop of the prepared Fe@AgNPs-AETrGO solution was placed on a clear glass sheet and then dried in air.

A Rigaku Miniflex X-ray diffractometer (Japan) was used for X-ray diffraction measurements of the material nanostructures. A scanning speed of $2\theta=2°$/min with a step size of 0.02° was used to examine the samples in a range of 5–75°.

Preparation of Fe@AgNPs

To synthesize the Fe@AgNPs, 0.01 M $Fe(NO_3)_3$ (4 mL) was prepared by diluting the $Fe(NO_3)_3$ solution with ultra-pure water and reduced by mixing with ascorbic acid solution at a concentration of 0.1 M (20 mL) at around 25 °C under a nitrogen flow for 20 min. After pH of the solution was adjusted to 4.0, 0.01 M $AgNO_3$ (4 mL) solution was slowly added in 1 h. A dark solid solution showed that the silver shell was coating on the iron core. Then, a magnet was used to separate the solid and the product was further washed several times with distilled water.

Synthesis of rGO

Graphene oxide (GO) was prepared by the modified Hummers method [38, 39]. Typically, 2.5 g of graphite powder was placed in a flask containing a mixture of 12.5 mL of H_2SO_4 (98 %), 2.5 g of $K_2S_2O_8$, and 2.5 g of P_2O_5. The mixture was kept at 80 °C for 6 h. Then, the mixture was cooled to room temperature and diluted with 500 mL of ultra-pure water. The product was filtered and washed with ultra-pure water and 125 mL of H_2SO_4 (98 %) was added at 0 °C. After that, 15 g of $KMnO_4$ were added to the stirring suspension which was kept at 20 °C. After the feeding of $KMnO_4$ was finished, the flask was heated to 50 °C. After 4 h, 500 mL of ultra-pure water was added to the mixture in an ice bath. The last mixture was stirred for 2 h and diluted to 1 L with ultra-pure water. After that, the suspension was fed slowly with 20 mL of H_2O_2 (30 %) and the solution started bubbling. The color of the suspension changed to brilliant yellow from brownish. The synthesized graphene oxide was filtered and washed with 0.1 M HCl and ultra-pure water three times. The graphene oxide was collected by an ultracentrifuge.

The as-prepared GO was dispersed into 200 mL water. After that, 4 mL of hydrazine hydrate (80 wt%) was added and the solution was heated in an oil bath at 100 °C under a water-cooled condenser for 24 h. After the reaction, the prepared rGO product was collected by vacuum filtration.

Preparation of Fe@AgNPs-AETrGO composite

The preparation of Fe@AgNPs-AETrGO composite is shown in Scheme 1. Firstly, rGO was dissolved in ethanol at 2 mg mL^{-1}. The mixture was sonicated to form a homogeneous suspension. The prepared rGO suspension was treated with 0.2 M of EDC solution for 8 h to ensure the surface activation of residual carboxylated groups. EDC is the most popular compound for labeling or crosslinking to free carboxylic groups on rGO [40]. EDC can react with carboxylic acid groups to form an active intermediate product that is easily displaced by nucleophilic attack from primary amino groups in the

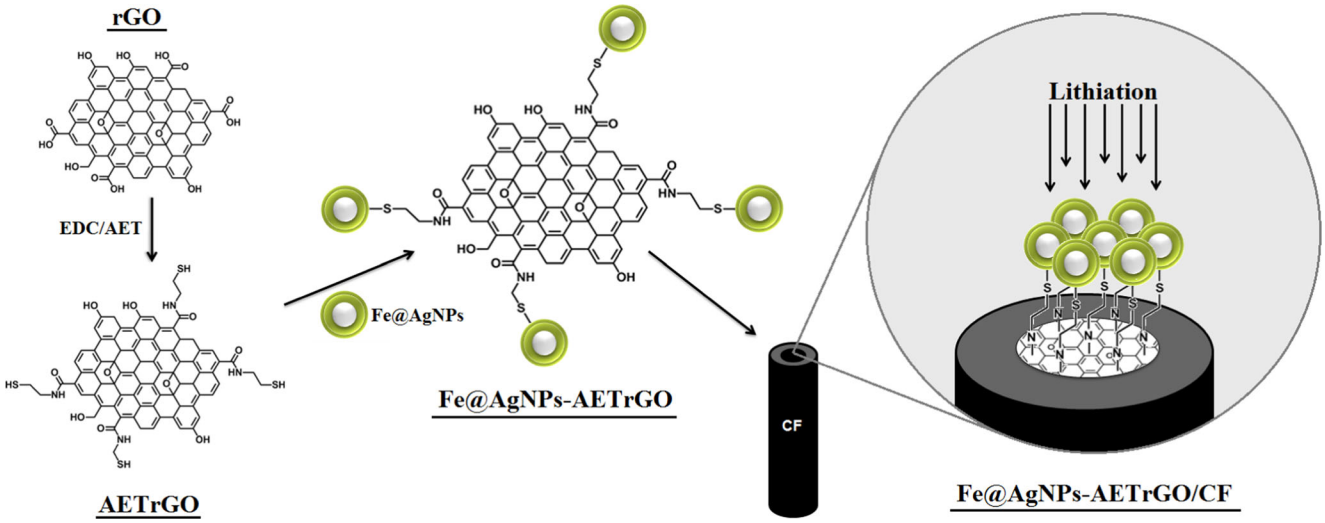

Scheme 1 Schematic diagram of the synthesis and modification of Fe@AgNPs-AETrGO composite on Cu foil and lithiation/delithiation sites

reaction mixture. Therefore, we used EDC for activation of free carboxylic acid groups of rGO. Then 1.0 mM AET was mixed with the activated rGO suspension at a 1:1 volume ratio and kept stirring for 2 h (AETrGO). After that, 1 mg mL^{-1} of Fe@AgNPs solution was mixed with the 0.1 mg mL^{-1} of AETrGO solution at a 1:1 volume ratio. Finally, the mixture was sonicated to generate a homogeneous mixture (Fe@AgNPs-AETrGO).

Electrochemical measurements

The electrochemical tests of rGO, Fe@AgNPs, and Fe@AgNPs-AETrGO composite as anode materials were investigated using CR2032 coin-type cells. $LiPF_6$ was used as an electrolyte solution in all the tests. The materials were prepared and attached on cells in an Ar-filled glove box. The rGO, Fe@AgNPs, and Fe@AgNPs-AETrGO composite were respectively mixed with carbon black at a weight ratio of 8:1 to enhance the conductivity for each material. NMP was used as a solvent to make a slurry mixture. The mixtures were pasted uniformly onto Cu foils (CF) as anode electrodes and the cathode electrode was a Li metal foil. The scan rate was 50 mV s^{-1} for the electrochemical performances. The reference electrode was Ag/AgCl/KCl(sat) in aqueous media. The process of lithiation/delithiation of Fe@AgNPs-AETrGO/Cu electrode is shown in Scheme 1. The anode electrodes were dried at 70 °C in a vacuum oven and pressed under a pressure around 10 MPa. Celgard 2600 was used as a separator. The electrochemical performances of rGO, Fe@AgNPs, and Fe@AgNPs-AETrGO electrodes were investigated by galvanostatic charge–discharge measurements with a computer-controlled battery tester at room temperature between the voltage ranges of 3.0–0.1 V.

Results and discussion

Characterization of Fe@AgNPs-AETrGO nanocomposite

The morphology of Fe@AgNPs-AETrGO composite is shown in Fig. 1. Figure 1a presents transmission electron microscopy (TEM) image of the spherical shaped Fe@AgNPs with an average diameter of 15–30 nm on rGO sheets. It can be seen that the Fe@AgNPs have been distributed on the rGO sheets. Figure 1b and Fig. 1c show SEM images of the bare Cu foil and Cu surface modified by Fe@AgNPs-AETrGO, respectively. Figure 1c shows that the Fe@AgNPs-AETrGO composite has successfully modified Cu foil surface. The layered structure of the Fe@AgNPs-AETrGO composite can be seen clearly from Fig 1c.

The structure of Fe@AgNPs-AETrGO composite was also determined by X-ray diffraction (XRD) measurements (Fig. 2). The intense and narrow peak at 2θ=22.1° refers to the (002) plane of rGO sheets [41] and the weak peaks at 2θ= 32.4° and 45.1° were also found corresponding to (101) and (004) planes of rGO sheets, respectively [42]. The characteristic peaks of Fe@AgNPs also have been observed. The two main peaks for the (110) and (220) planes of Fe at 2θ=44.2° and 65.3° are overlapped with the (200) and (220) planes of Ag, respectively [43]. The peak at 2θ=77.4° is the (311) plane of Ag.

XPS results (Fig. 3) were obtained to examine the formation of Fe@AgNPs-AETrGO composite. The C1s core-level spectrum was curve-fitted, and the peaks at 282.8, 284.3, and 285.7 eV were corresponded to C-H, C-N, and -CONH, respectively. S2p spectrum was curve-fitted with two components by a doublet $2p^{1/2}$ and $2p^{3/2}$ signals. The peak at 163.2 eV confirmed that the silver nanoparticles were grafted to S atoms. The peak observed at 162.3 eV has shown the unreacted thiol group of AET [31]. N1s narrow region

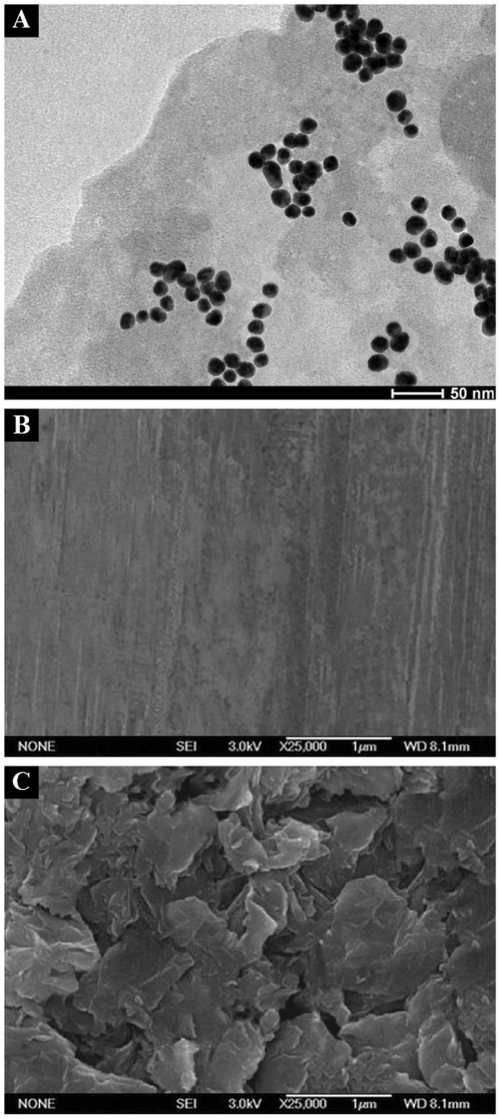

Fig. 1 **a** TEM image of Fe@AgNPs-AETrGO composite; **b** SEM images of bare Cu foil; and **c** Fe@AgNPs-AETrGO/Cu electrode

spectrum was curve-fitted and the peak at 398.6 eV was corresponded to the N-H groups of amide that forms due to the reaction of rGO's carboxyl groups and AET's amino groups. The peak at 401.2 eV was assigned to the unreacted N-H groups of AET. Ag3d curve is characterized by a doublet $3d^{5/2}$ and $3d^{3/2}$ signals at 366.2 and 372.1 eV, respectively, indicating the existence of Ag [44, 45]. The presence of iron nanoparticles has been shown from the peaks of Fe $2p^{1/2}$ and Fe $2p^{3/2}$ at 722.5 and 711.4 eV, respectively [46].

Electrochemical performance Fe@AgNPs-AETrGO in LIB

The rate capability of a battery can be affected by various factors such as charge transfer resistance, mass-transfer resistance, and ohmic resistance. It is generally known that small-sized nanoparticles deposited on carbon materials such as rGO provide high specific surface area and fast redox reactions, which can reduce the charge transfer resistance [47].

The curves of first cycle charge and discharge of rGO, Fe@AgNPs, and Fe@AgNPs-AETrGO anodes at 0.1 C rate between 0.01 and 3.0 voltages of Li^+/Li are shown in Fig. 4. The Fe@AgNPs anode shows specific charge capacity of 641 mAh g^{-1} and discharge capacity of 348 mAh g^{-1}. The specific charge capacity of Fe@AgNPs-AETrGO anode is at 2185 mAh g^{-1}, which is much higher than that of rGO and Fe@AgNPs. This indicates that the Fe@AgNPs-AETrGO composite significantly reduced the diffusion resistance of the lithium ions in the $LiPF_6$ electrolyte and increased the specific capacities and conductivity of the electrode [48, 49]. The presence of Fe@AgNPs can increase the layer gap of the rGO, making high Li-ion adsorption and reducing diffusion resistance of lithium ion. In addition, the rGO support increased the conductivity of the composite material.

Figure 5 represents initial 50 charge/discharge curves at 0.1 C rate corresponding to 100 mA g^{-1} of the as-prepared Fe@AgNPs-AETrGO anode in coin-type test cells using lithium foil as the counter and reference electrodes between 0.01 and 3.0 V (vs. Li^+/Li). In Fig. 5, a voltage plateau around 0.74 V (vs. Li/Li^+) and the specific capacity at 2185 mAh g^{-1} were observed at the first lithiation, corresponding to the electrolyte decomposition and solid electrolyte interface (SEI) formation [50]. The SEI layer was a multilayer structure with a thickness of 100–150 nm. The thickness of Cu foil was 18 μm and the thickness of anode electrode was controlled at the same value. Due to the thin SEI layer, the Fe@AgNPs-AETrGO/Cu electrode has a large specific surface area. As seen in Fig. 5, the large irreversible capacity loss after the 1st cycle is related to the large specific surface area of Fe@AgNPs-AETrGO composite and the SEI on the electrode [51]. The maximum theoretical capacities for rGO and Fe@AgNPs are about 562 and 641 mAh g^{-1}, respectively. The irreversible capacity of the Fe@AgNPs-AETrGO anode in the first cycle is much higher than the theoretical capacities of rGO and Fe@AgNPs. The extra capacity for the first cycle

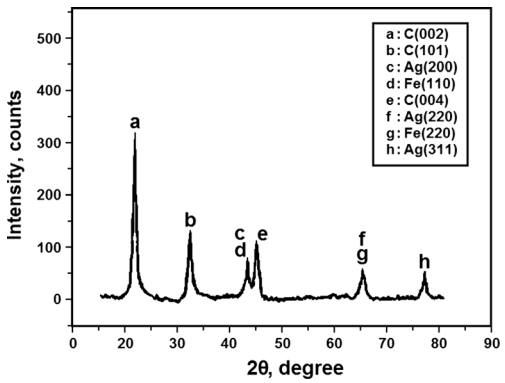

Fig. 2 XRD pattern of the Fe@AgNPs-AETrGO composite

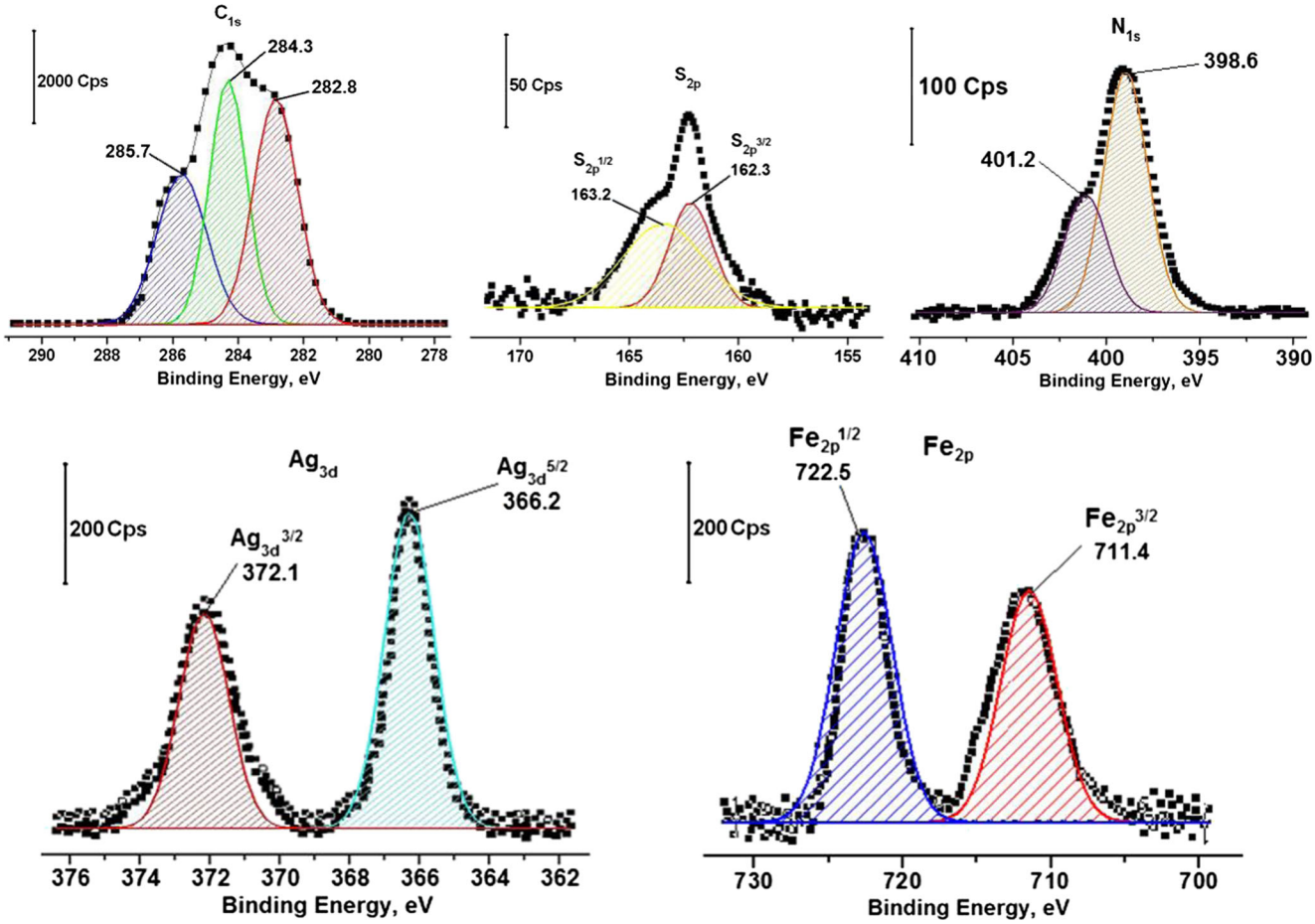

Fig. 3 XPS spectra of Fe@AgNPs-AETrGO composite

over theoretical value is attributed to the formation of SEI film on the surface of Fe@AgNPs-AETrGO composite. Another reason is the presence of abundant unsaturated carbon atoms on the Fe@AgNPs-AETrGO composite, which may catalyze the electrolyte decomposition [52].

The electrochemical behaviors of the Fe@AgNPs-AETrGO in Li-ion cell in the initial 50 cycles were displayed in Fig. 6 [53, 54]. The anodic scan shows two peaks at 1995 and 2315 mV, respectively, which correspond to the oxidation reactions of Fe^0 to Fe^{2+} and Ag^0 to Ag^+, respectively. From the 1st to the 50th cycle, slight changes in the current densities and the positions of the oxidation peaks are attributed to polarization due to the electronic resistance of active Fe@AgNPs-AETrGO composite. In addition, the interfacial kinetic resistance against intercalation/extraction represents that the composite electrode has good irreversibility of the oxidation reactions of Fe^0 to Fe^{2+} and Ag^0 to Ag^+. On the other hand, the cathodic scan resulted in mainly two peaks at

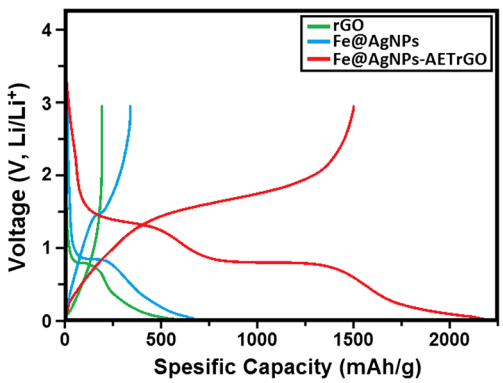

Fig. 4 Typical charge/discharge curves at 0.1 C of rGO, Fe@AgNPs, and Fe@AgNPs-AETrGO as anode for the first cycle

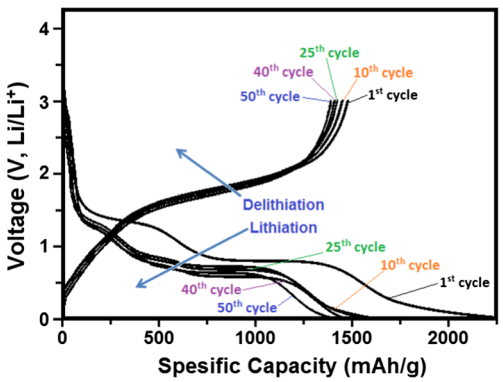

Fig. 5 Typical charge/discharge curves at 0.1 C of Fe@AgNPs-AETrGO as anode for the first 50 cycles

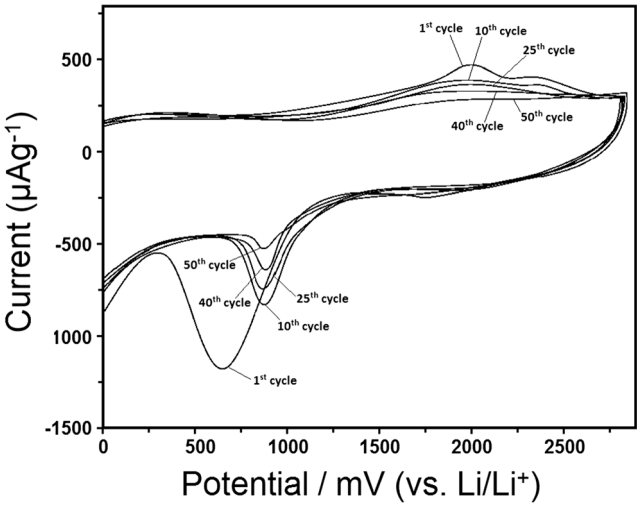

Fig. 6 Cyclic voltammogram curves of the Fe@AgNPs-AETrGO anode material for the initial 50 cycles

695 and 805 mV, respectively, and these peaks can be attributed to the electrochemical reduction of Fe^{2+} and Ag^{+} ions, respectively, with lithium in the electrode. It is clearly seen that there is a difference between the first and the subsequent cycles. For the first cycle, a sharp cathodic peak appears at about 695 mV, which is associated with the electrolyte decomposition to form SEI films [55] and the reduction of Fe^{2+} to Fe^{0}. In the subsequent cycles, this strong peak completely decreased, indicating no more irreversible SEI formation of electrolyte. From the subsequent cycles, the redox peaks occur at around 805 mV, attributed to the irreversible electrochemical reduction of Fe^{2+} and Ag^{+} ions with lithium in the electrode.

The capacity value of 1500 mAh g^{-1} for Fe@AgNPs-AETrGO composite is much higher than that of the Fe@AgNPs and rGO. This suggests that there is obviously synergistic effect between Fe@AgNPs and rGO. Such high charge–discharge specific capacity of the Fe@AgNPs-AETrGO electrode indicates that the contact between Fe@AgNPs and rGO is very efficient to resist the changes in the volume of Fe@AgNPs. The rGO provides the cushion-like effect during lithium ion insertion and desertion, and thus contributes greatly to the enhancement of electrochemical property. The remarkable performance reveals the beneficial effects of well-deposited Fe@AgNPs on the rGO surface. Furthermore, the enhanced lithium storage properties can be also attributed to the small effective diffusion length associated with the well-dispersed Fe@AgNPs with small particle size on the rGO surface. The ability to charge and discharge Li-ion batteries at higher rate is important in practical use.

We also have investigated the electrochemical performance of rGO, Fe@AgNPs, and Fe@AgNPs-AETrGO electrodes by changing rates of charge–discharge current densities. Figure 7 shows the specific capacities of rGO, Fe@AgNPs, and

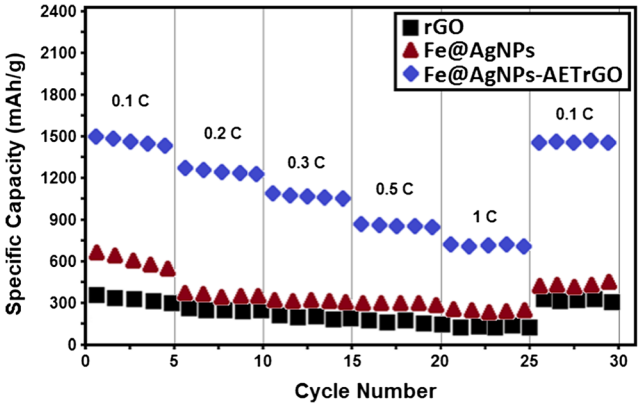

Fig. 7 The rate capability of Fe@AgNPs-AETrGO, Fe@AgNPs, and rGO electrodes

Fe@AgNPs-AETrGO in a range of 0.1–1.0 C. The capacity decreased with increasing charge/discharge rate and the specific capacity of 718 mAh g^{-1} was measured at a current rate of 1.0 C for Fe@AgNPs-AETrGO material. On the other hand, the specific capacity decreases quickly at 0.1 C current rate for the Fe@AgNPs and it was observed as 112 mAh g^{-1} for the current rate of 1.0 C. The capacity of 137 mAh g^{-1} for the rGO electrode was observed at the same rate. The grafting of Fe@AgNPs on the surface of rGO provides positive effects such as increasing the stability of Fe@AgNPs and active groups of the Fe@AgNPs on the surface for Li ions. Figure 7 also shows that, when the current rate decreases to 0.1 C, the capacities of the three samples restore almost the original amounts, which suggests that the three samples all have excellent circulation property. Moreover, the capacities of the three samples were quite stable at the high 1 C rate, indicating good lithium ion diffusivity in the three samples.

According the electrochemical test results, the properties of the improved lithium storage resulted from the smaller diffusion length of lithium and the well-dispersed Fe@AgNPs on rGO sheets. The rGO sheets as a support have good dispersion and increase stability of the Fe@AgNPs. Hence, the well-dispersed Fe@AgNPs may assure a smaller and effective diffusion length improving the performance of LIBs. As a result, high lithium storage and great cycling and rate performance are realized by the Fe@AgNPs-AETrGO composite. Additionally, the stability of the Cu foil modified with Fe@AgNPs-AETrGO was also investigated. After 1 month, the current response is maintaining at approximate 95.48 % of the original value, suggesting the very promising performance for the future of Li-ion batteries.

Conclusion

In this study, we synthesized Fe@AgNPs on AET functionalized rGO and characterized their properties using TEM, XPS, SEM, and XRD. The synthesized Fe@AgNPs-AETrGO

composite as an anode material in LIBs significantly improves the performance and remains stable even after 50 cycles. The Fe@AuNPs-AETrGO composite showed a high specific gravimetric capacity of about 1500 mAh g^{-1} and long-term cycle stability. The highly improved electrochemical performance of Fe@AgNPs-AETrGO composite is attributed to the small size and dispersion of Fe@AgNPs on rGO sheets. This study demonstrates that the rGO support plays significant roles in improving the storage capacity, cycle life, and rate capability of the anode electrode by avoiding the aggregation of Fe@AgNPs and working as a substrate for lithium insertion/desertion.

Acknowledgments We thank the Australia Research Council for partially financial support under Project No: DP150103026.

References

1. Scrosati B, Garche J (2010) Lithium batteries: status, prospects and future. J Power Sources 195(9):2419–2430
2. Gupta VK, Yola ML, Atar N, Ustundağ Z, Solak AO (2013) A novel sensitive Cu(II) and Cd(II) nanosensor platform: graphene oxide terminated p-aminophenyl modified glassy carbon surface. Electrochimica Acta 112:541–548
3. Kim MG, Cho J (2009) Reversible and high-capacity nanostructured electrode materials for Li-ion batteries. Adv Funct Mater 19(10):1497–1514
4. Lee J, Kumar P, Lee J, Moudgil BM, Singh RK (2013) ZnO incorporated $LiFePO_4$ for high rate electrochemical performance in lithium ion rechargeable batteries. J Alloys Compd 550:536–544
5. Li Z, Wang L, Li K, Xue D (2013) $LiMn_2O_4$ rods as cathode materials with high rate capability and good cycling performance in aqueous electrolyte. J Alloys Compd 580:592–597
6. Park H (2013) A design of air flow configuration for cooling lithium ion battery in hybrid electric vehicles. J Power Sources 239:30–36
7. Liu Y, Liu D, Zhang Q, Cao G (2011) Engineering nanostructured electrodes away from equilibrium for lithium-ion batteries. J Mater Chem 21(27):9969–9983
8. Wu ZS, Zhou GM, Yin LC, Ren W, Li F, Cheng HM (2012) Graphene/metal oxide composite electrode materials for energy storage. Nano Energy 1(1):107–131
9. Li HQ, Zhou HS (2012) Enhancing the performances of Li-ion batteries by carbon-coating: present and future. Chem Commun 48(9):1201–1217
10. W. A. van Schalkwijk BS (2002) Advances in lithium-ion batteries, vol Chapter 2. Kluwer Academic, New York
11. Shafiei M, Alpas AT (2011) Electrochemical performance of a tin-coated carbon fibre electrode for rechargeable lithium-ion batteries. J Power Sources 196(18):7771–7778
12. Li X, Zhong Y, Cai M, Balogh MP, Wang D, Zhang Y, Li R, Sun X (2013) Tin-alloy heterostructures encapsulated in amorphous carbon nanotubes as hybrid anodes in rechargeable lithium ion batteries. Electrochimica Acta 89:387–393
13. Yue W, Yang S, Liu Y, Yang X (2013) A facile synthesis of mesoporous graphene-tin composites as high-performance anodes for lithium-ion batteries. Mater Res Bull 48(4):1575–1580
14. Su L, Jing Y, Zhou Z (2011) Li ion battery materials with core-shell nanostructures. Nanoscale 3(10):3967–3983
15. Novoselov KS, Fal'ko VI, Colombo L, Gellert PR, Schwab MG, Kim K (2012) A roadmap for graphene. Nature 490(7419):192–200
16. Robinson JT, Perkins FK, Snow ES, Wei Z, Sheehan PE (2008) Reduced graphene oxide molecular sensors. Nano Letters 8(10):3137–3140
17. Jung YU, S-i O, Choa S-H, Kim H-K, Kang SJ (2013) Electromechanical properties of graphene transparent conducting films for flexible electronics. Curr Appl Phys 13(7):1331–1334
18. Yu S, Jiang Y, Wang C (2013) A polymer composite consists of electrochemical reduced graphene oxide/polyimide/chemical reduced graphene oxide for effective preparation of SnSe by electrochemical atomic layer deposition method with enhanced electrochemical performance and surface area. Electrochimica Acta 114:430–438
19. Zhang Y, Wang S, Li L, Zhang K, Qiu J, Davis M, Hope-Weeks LJ (2012) Tuning electrical conductivity and surface area of chemically-exfoliated graphene through nanocrystal functionalization. Mater Chem Phys 135(2–3):1057–1063
20. Gupta VK, Yola ML, Eren T, Atar N (2015) Selective QCM sensor based on atrazine imprinted polymer: its application to wastewater sample. Sensors and Actuators, B: Chemical 218:215–221
21. Karimi-Maleh H, Tahernejad-Javazmi F, Atar N, Yola ML, Gupta VK, Ensafi AA (2015) A novel DNA biosensor based on a pencil graphite electrode modified with polypyrrole/functionalized multiwalled carbon nanotubes for determination of 6-mercaptopurine anticancer drug. Ind Eng Chem Res 54(14):3634–3639
22. Gupta VK, Yola ML, Atar N, Üstündağ Z, Solak AO (2014) Electrochemical studies on graphene oxide-supported metallic and bimetallic nanoparticles for fuel cell applications. J Mol Liq 191:172–176
23. Jain R, Gupta VK, Jadon N, Radhapyari K (2010) Voltammetric determination of cefixime in pharmaceuticals and biological fluids. Anal Biochem 407(1):79–88
24. Goyal RN, Gupta VK, Chatterjee S (2008) Simultaneous determination of adenosine and inosine using single-wall carbon nanotubes modified pyrolytic graphite electrode. Talanta 76(3):662–668
25. Gupta VK, Jain S, Chandra S (2003) Chemical sensor for lanthanum(III) determination using aza-crown as ionophore in poly(vinyl chloride) matrix. Anal Chim Acta 486(2):199–207
26. Goyal RN, Gupta VK, Bachheti N (2007) Fullerene-C60-modified electrode as a sensitive voltammetric sensor for detection of nandrolone—an anabolic steroid used in doping. Anal Chim Acta 597(1):82–89
27. Gupta VK, Jain AK, Maheshwari G, Lang H, Ishtaiwi Z (2006) Copper(II)-selective potentiometric sensors based on porphyrins in PVC matrix. Sensors and Actuators B: Chemical 117(1):99–106
28. Gupta VK, Eren T, Atar N, Yola ML, Parlak C, Karimi-Maleh H (2015) $CoFe_2O_4$@TiO_2 decorated reduced graphene oxide nanocomposite for photocatalytic degradation of chlorpyrifos. J Mol Liq 208:122–129
29. Zeng Z, Zhao H, Wang J, Lv P, Zhang T, Xia Q (2014) Nanostructured Fe3O4@C as anode material for lithium-ion batteries. J Power Sources 248:15–21
30. Ye Y-S, Xie X-L, Rick J, Chang F-C, Hwang B-J (2014) Improved anode materials for lithium-ion batteries comprise non-covalently bonded graphene and silicon nanoparticles. J Power Sources 247:991–998
31. Gupta VK, Atar N, Yola ML, Üstündağ Z, Uzun L (2014) A novel magnetic Fe@Au core–shell nanoparticles anchored graphene oxide recyclable nanocatalyst for the reduction of nitrophenol compounds. Water Res 48:210–217
32. Li N, Chen Z, Ren W, Li F, Cheng H-M (2012) Flexible graphene-based lithium ion batteries with ultrafast charge and discharge rates. Proc Natl Acad Sci 109(43):17360–17365

33. Wang G, Shen X, Yao J, Park J (2009) Graphene nanosheets for enhanced lithium storage in lithium ion batteries. Carbon 47(8): 2049–2053
34. Ghosh Chaudhuri R, Paria S (2011) Core/shell nanoparticles: classes, properties, synthesis mechanisms, characterization, and applications. Chem Rev 112(4):2373–2433
35. Gupta VK, Yola ML, Eren T, Kartal F, Çağlayan MO, Atar N (2014) Catalytic activity of Fe@Ag nanoparticle involved calcium alginate beads for the reduction of nitrophenols. J Mol Liq 190: 133–138
36. Daniel M-C, Astruc D (2003) Gold nanoparticles: assembly, supramolecular chemistry, quantum-size-related properties, and applications toward biology, catalysis, and nanotechnology. Chem Rev 104(1):293–346
37. Qi L, Ma J, Cheng H, Zhao Z (1996) Synthesis and characterization of mixed CdS ZnS nanoparticles in reverse micelles. Colloids and Surfaces A: Physicochemical and Engineering Aspects 111(3):195–202
38. Dreyer DR, Park S, Bielawski CW, Ruoff RS (2010) The chemistry of graphene oxide. Chem Soc Rev 39(1):228–240
39. Kovtyukhova NI, Ollivier PJ, Martin BR, Mallouk TE, Chizhik SA, Buzaneva EV, Gorchinskiy AD (1999) Layer-by-layer assembly of ultrathin composite films from micron-sized graphite oxide sheets and polycations. Chem Mat 11(3):771–778
40. Yola ML, Eren T, Atar N (2014) Molecularly imprinted electrochemical biosensor based on Fe@Au nanoparticles involved in 2-aminoethanethiol functionalized multi-walled carbon nanotubes for sensitive determination of cefexime in human plasma. Biosens Bioelectron 60:277–285
41. Stobinski L, Lesiak B, Malolepszy A, Mazurkiewicz M, Mierzwa B, Zemek J, Jiricek P, Bieloshapka I (2014) Graphene oxide and reduced graphene oxide studied by the XRD, TEM and electron spectroscopy methods. J Electron Spectrosc Relat Phenom 195: 145–154
42. Bradder P, Ling SK, Wang S, Liu S (2010) Dye adsorption on layered graphite oxide. J Chem Eng Data 56(1):138–141
43. Haw-Yeu C, Dong-Hwang C (2009) Fabrication and photocatalytic activities in visible and UV light regions of Ag@TiO 2 and NiAg@TiO 2 nanoparticles. Nanotechnology 20(10):105704
44. Yola ML, Gupta VK, Eren T, Şen AE, Atar N (2014) A novel electro analytical nanosensor based on graphene oxide/silver nanoparticles for simultaneous determination of quercetin and morin. Electrochim Acta 120:204–211
45. Gupta VK, Atar N, Yola ML, Darcan C, Idil Ö, Üstünda Z, Suhas (2013) Biosynthesis of silver nanoparticles using chitosan immobilized *Bacillus cereus*: nanocatalytic studies. J Mol Liq 188:81–88
46. Grosvenor AP, Kobe BA, Biesinger MC, McIntyre NS (2004) Investigation of multiplet splitting of Fe 2p XPS spectra and bonding in iron compounds. Surf Interface Anal 36(12):1564–1574
47. Kim J, Chung MK, Ka BH, Ku JH, Park S, Ryu J, Oh SM (2010) The role of metallic Fe and carbon matrix in Fe_2O_3/Fe/carbon nanocomposite for lithium-ion batteries. J Electrochem Soc 157(4): A412–A417
48. Du J, Chen C-H (2012) Structure and lithium ion diffusion in lithium silicate glasses and at their interfaces with lithium lanthanum titanate crystals. J Non-Cryst Solids 358(24):3531–3538
49. Han S-W, Jung D-W, Jeong J-H, Oh E-S (2014) Effect of pyrolysis temperature on carbon obtained from green tea biomass for superior lithium ion battery anodes. Chem Eng J 254:597–604
50. Cheng C-S, Liu W-R, Wang F-M (2013) A novel ionic host solid electrolyte interface formation on reduced graphene oxide of lithium ion battery. Electrochim Acta 106:425–431
51. Xiao XC, Liu P, Wang JS, Verbrugge MW, Balogh MP (2011) Vertically aligned graphene electrode for lithium ion battery with high rate capability. Electrochem Commun 13(2):209–212
52. Webb SA, Baggetto L, Bridges CA, Veith GM (2014) The electrochemical reactions of pure indium with Li and Na: anomalous electrolyte decomposition, benefits of FEC additive, phase transitions and electrode performance. J Power Sources 248:1105–1117
53. Mustansar Abbas S, Tajammul Hussain S, Ali S, Ahmad N, Ali N, Abbas S, Ali Z (2013) Modification of carbon nanotubes by CuO-doped NiO nanocomposite for use as an anode material for lithium-ion batteries. J Solid State Chem 202:43–50
54. Zhao S, Bai Y, Chang Q, Yang Y, Zhang W (2013) Surface modification of spinel $LiMn_2O_4$ with FeF_3 for lithium ion batteries. Electrochim Acta 108:727–735
55. Xiao W, Wang Z, Guo H, Li X, Wang J, Huang S, Gan L (2013) Fe_2O_3 particles enwrapped by graphene with excellent cyclability and rate capability as anode materials for lithium ion batteries. Appl Surf Science 266:148–154